Geochemical Perspectives Letters

A two stage impact melting process in an impact glass strewn field from the Atacama Desert

P. Rochette[1*], G. Di Vincenzo[2], J. Gattacceca[1], J.A. Barrat[3], B. Devouard[1], L. Folco[4], A. Musolino[1], Y. Quesnel[1]

https://doi.org/10.7185/geochemlet.2418

Abstract

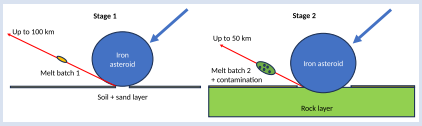

A new type of silica-rich glass has been discovered associated with the known impact glass strewn field of the Atacama Desert. Based on petrography, chemical composition and indistinguishable $^{40}Ar/^{39}Ar$ formation ages at *circa* 6.6 Ma, we infer that these two glasses were produced by the same impact event, which gave rise to two successive compositionally different melt batches in close succession. The first one is a silica-rich melt derived from a mixture of quartz sand and weathered magmatic rocks. It is reduced and devoid of extraterrestrial contamination. The second one, much more abundant and which corresponds to the normal glass, is oxidised, highly contaminated by the iron type impactor and derived from an underlying unweathered dacitic rock. This scheme sheds a new light on the first second of the interaction between the Earth surface and a large metallic asteroid.

Received 16 December 2023 | Accepted 3 April 2024 | Published 3 May 2024

Introduction

Hypervelocity impacts on the Earth surface produce melts that can be ejected away from the crater (Glass and Simonson, 2013) at distance varying from 0.1 to less than 100 km for proximal ejecta or from 200 to 10,000 km for distal ejecta, such as tektites. Chemical and isotopic compositions of these melts may reflect provenance from the upper layers of the crust (Ma *et al.*, 2004; Rochette *et al.*, 2018), more or less contaminated by the extraterrestrial impactor (Koeberl, 2014), and showing variable compositions mimicking the heterogeneity of the target. Exploring the variabilities in the melt composition, target depth, and meteoritic contamination may help to understand details in the initial interactions between the impactor and the Earth surface. Such interactions have been already explored experimentally (Ebert *et al.*, 2014), in proximal ejecta around small craters (Hamann *et al.* 2018; Folco *et al.*, 2022), and in the largest ejecta known on Earth, the australasian tektite field (Folco *et al.*, 2023).

We recently described an impact glass strewn field extending over 50 km along a N120° azimuth in the Atacama Desert (Gattacceca *et al.*, 2021; Fig. 1). These black glasses, named atacamaites, are found as small splash-forms (average and maximum mass of 0.55 and 5.9 g, respectively), of dacitic composition. Their elemental and isotopic composition is compatible with an origin from local Andean magmatic rocks. The source crater has not been identified so far, but it was estimated to be relatively proximal (less than *circa* 100 km from the strewn field), based on the strong differences between atacamaites and *bona fide* tektites (see discussion in Gattacceca *et al.*, 2021). In particular atacamaites show a relatively strong contamination by an iron meteorite impactor (likely IIAB type), on average 5 wt. % and up to 9 wt. %. They also contain a significant amount of magnetite, indicative of a large Fe^{3+}/Fe_{tot} ratio. The fission track dating method was used to obtain a preliminary late Miocene age estimate.

A distal NW satellite of the main strewn field (Fig. 1) was briefly reported in Gattacceca *et al.* (2021). In that distinct area, extending away for over 50 km, rare small glass teardrops are found. Because of their distinctive light brown colour and translucent lustre, pointing toward a different bulk composition than the normal black and opaque atacamaites, one may challenge the hypothesis that they derive from the same impact. Studying this different glass type, hereafter named silica-rich glass, and comparing it to the normal atacamaites is the purpose of the present contribution. Methods used are described in Supplementary Information.

This glass strewn field is quite unique in the terrestrial record by being intermediate between proximal and distal glass ejecta, suggesting it may bring original clues on the impact melting and ejecta processes.

Results and Interpretation

Field work and petrography. In the satellite strewn field, we collected while searching for meteorites 25 translucent glass samples labelled EM in the El Medano dense collection area (DCA; Hutzler *et al.*, 2016), one sample in Caleta el Cobre DCA (labelled CEC) 25 km north of EM, and two samples 15 km southeast of

1. Aix-Marseille Université, CNRS, IRD, INRAE, CEREGE, Aix en Provence, France
2. Istituto di Geoscienze e Georisorse – CNR, via G. Moruzzi 1, 56124 Pisa, Italy
3. Univ Brest, CNRS, Ifremer, IRD, LEMAR, Plouzané, France
4. Dipartimento di Scienze della Terra, Università di Pisa, V. S. Maria 53, 56126, Pisa, Italy
* Corresponding author (email: rochette@cerege.fr)

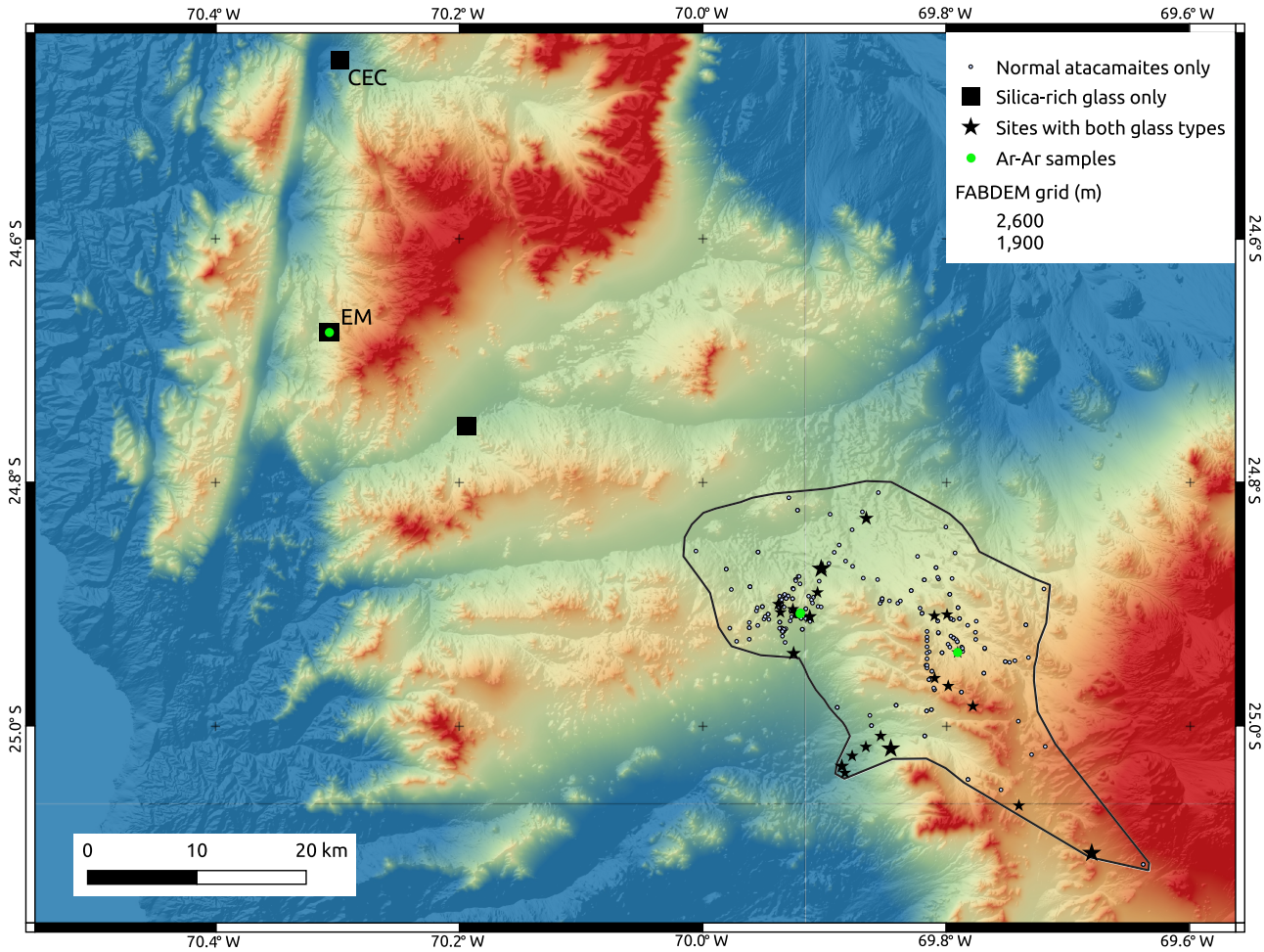

Figure 1 Map of the normal atacamaite strewn field, surrounded by a solid black line, together with locations of the silica-rich glass. Large stars correspond to sites with the largest proportion of silica-rich samples.

EM. Median and maximum sample masses are 0.16 and 0.78 g, respectively. Magnetic susceptibilities (χ) values range from 43 to 87×10^{-9} m^3/kg. If one excludes the three samples with masses well below 90 mg this range reduces to 69–80 $\times 10^{-9}$ m^3/kg, with a well-defined average of $76 \pm 3 \times 10^{-9}$ m^3/kg ($n = 25$). Electron probe microanalysis (EPMA) on six samples give similar values of SiO_2 and $Na_2O + K_2O$ at 85.8 ± 0.7 and 0.32 ± 0.3 wt. %, respectively (Table S-1). Most samples have abraded teardrop shapes, but a few (the largest) are irregularly shaped with large bubbles (Fig. S-1). Optical and scanning electron microscopy of polished samples shows pervasive flow textures, vesicles and lechatelierite (*i.e.* pure silica glass) inclusions, often as twisted ribbons.

In the main strewn field systematic susceptibility measurements and an optical check of translucent character identified site K260 of Gattacceca *et al.* (2021) as rich in similar material: 53 samples, *i.e.* about 20 % of total samples of this site, have translucent character and $\chi < 85 \times 10^{-9}$ m^3/kg. The average χ of this population is $77 \pm 4 \times 10^{-9}$ m^3/kg. Twenty four other sampling sites from Gattacceca *et al.* (2021) possess one to four samples with the same features. Maximum and median masses of these silica-rich samples in the main strewn field are 2.3 and 0.21 g, respectively. In total, 99 silica-rich samples were identified in the main strewn field, *i.e.* about 1 % of the total collection. A map of the main strewn field (Fig. 1) indicates that the silica-rich glasses are scattered across most of the strewn field, with a slight tendency for more frequent occurrences in the southwestern part.

One translucent sample from site K260 exhibits a higher susceptibility (169×10^{-9} m^3/kg), an anomaly attributable to a 1 mm large black spherical inclusion. A polished section through this inclusion shows a glass spherule typical of normal atacamaite material (*i.e.* enriched in Fe and Ni), embedded into silica-rich glass (Fig. S-1, Table S-1). This supports the idea that both glasses were welded within a hot spray.

Magnetic susceptibility measurements of the silica-rich glasses show values in agreement with the lack of magnetite and a purely paramagnetic susceptibility due to Fe^{2+} only (see Rochette *et al.*, 2015; Fig. S-2). The corresponding reduced character of this glass is further confirmed by a consistently negative loss on ignition (average −0.25 wt. %; Table S-2).

$^{40}Ar/^{39}Ar$ dating. Three samples from the normal glass (samples K51, K48G, K326) and one (EM1a) from the silica-rich type were analysed by the $^{40}Ar/^{39}Ar$ dating method using both the laser step heating and the laser total fusion techniques. Details on the analytical procedure are given in the Supplementary Information. Uncertainties are given at 2σ. Accuracy was checked by analysing fragments of moldavite VLTA2242 (Di Vincenzo, 2022). The full data set is listed in Table S-3.

Normal glass. All step heating experiments yielded reproducible flat or nearly flat age spectra, irrespective of the mass spectrometer utilised, with the exceptions of a few high temperature steps of data completed on samples K48G and K326 by the multi-collector noble gas mass spectrometer (Fig. S-3).

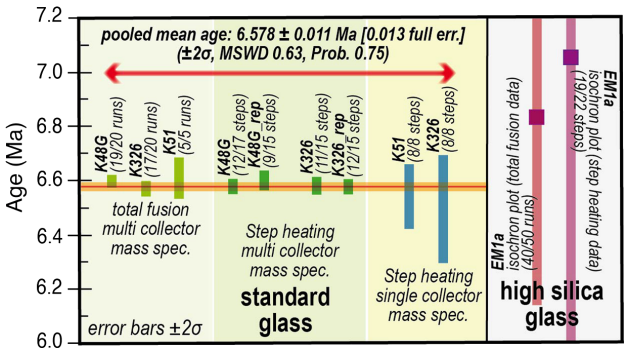

Figure 2 Summary of $^{40}Ar/^{39}Ar$ dates from step heating and total fusion data obtained in this study on normal glass (samples K48G, K326, K51) and a silica-rich glass (sample EM1a), through single and multi-collector mass spectrometers.

Concordant segments range from 65.3 to 100 % of the total $^{39}Ar_K$ released, with weighted mean dates indistinguishable within internal uncertainty, of 6.49 ± 0.20 to 6.60 ± 0.04 Ma (Fig. S-3). Data acquired using the multi-collector noble gas mass spectrometer yielded results with significantly lower analytical uncertainties and high temperature steps with apparent ages up to 6.7–7.0 Ma, suggestive of contamination by a minor extraneous Ar component (either excess or inherited Ar) heterogeneously distributed in the glass. Generally, total fusion data of single and a few glass fragments from the 0.35–0.50 mm grain fraction, in agreement with step heating data, gave mostly within sample concordant dates, ranging from 6.565 ± 0.028 to 6.605 ± 0.072 Ma (Fig. S-3). Combining intra-sample concordant $^{40}Ar/^{39}Ar$ data from step heating and total fusion data yields a pooled mean age of 6.578 ± 0.011 Ma (±0.013 including all known sources of errors; Fig. 2).

Silica-rich glass. Step heating data yielded statistically concordant age spectra for two aliquots of sample EM1a, although with some internal scatter, yielding indistinguishable apparent ages for the two aliquots of ~10 Ma (Fig. S-3). Analytical uncertainties are quite large when compared to $^{40}Ar/^{39}Ar$ data of the normal glass, because of the low gas yield due to the very low K contents of the high silica glass. Total fusion data of a few fragments of the same sample reveal instead a more complex picture, with single runs yielding apparent ages spanning over a large time interval of 7 to 14 Ma (Fig. S-3) most likely due an extraneous Ar component heterogeneously distributed in the glass. In an $^{36}Ar/^{40}Ar$ *versus* $^{39}Ar/^{40}Ar$ isochron diagram (Fig. S-4), both step heating and total fusion data define a triangular envelope which requires at least three distinct Ar components: (1) atmospheric Ar, (2) a radiogenic Ar component, located along the ordinate and yielding a date of ~6.5–7 Ma, and (3) extraneous Ar with a $^{40}Ar/^{36}Ar$ ratio of ~320. Selecting data points on the basis of their linearity and accepting linear regressions yielding a probability of fit ≥5 %, the triangular envelope defined by step heating data is defined toward the $^{39}Ar/^{40}Ar$ *x* axis by nineteen data points (Fig. S-4) that define a linear array (MSWD = 1.43) with an apparent intercept age of 7.1 ± 1.4 Ma

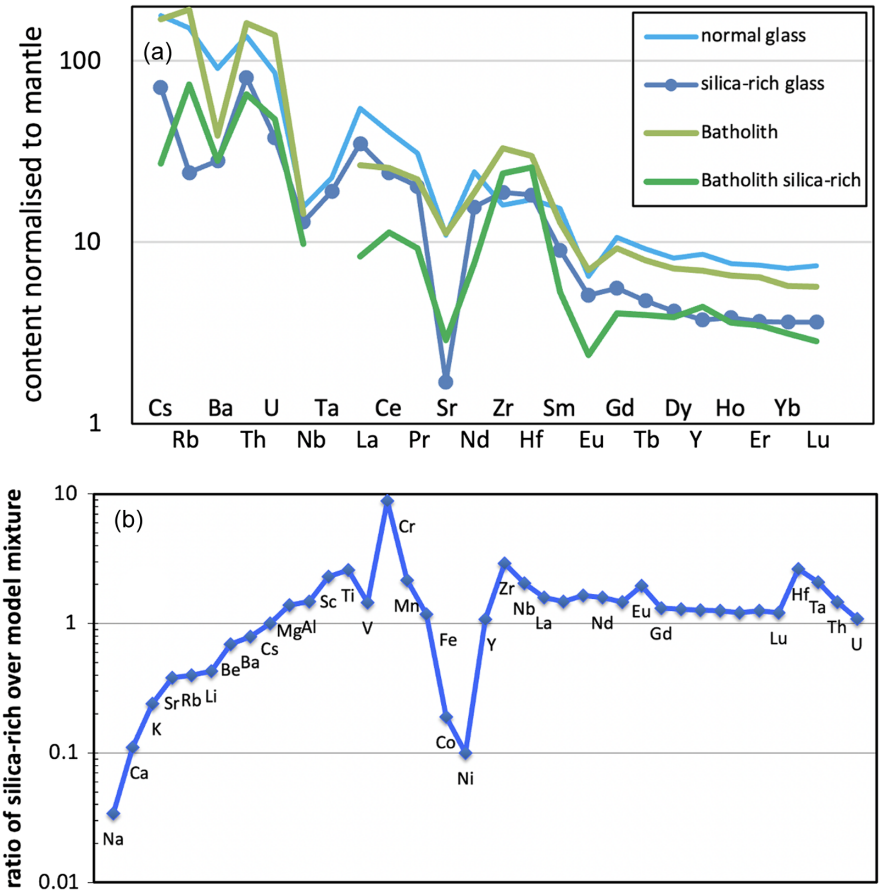

Figure 3 **(a)** Spidergram of trace elements normalised to primitive upper mantle (after McDonough and Sun, 1995) for the two glasses *versus* average coastal batholith data with SiO_2 content close to the glass and a compatible isotopic ratio (see Fig. S-5), **(b)** ratio of average composition of silica-rich glass to the average composition of normal glass corrected from quartz addition. Alkali elements appear first, ordered by increasing ratio, then the other elements with increasing atomic weight.

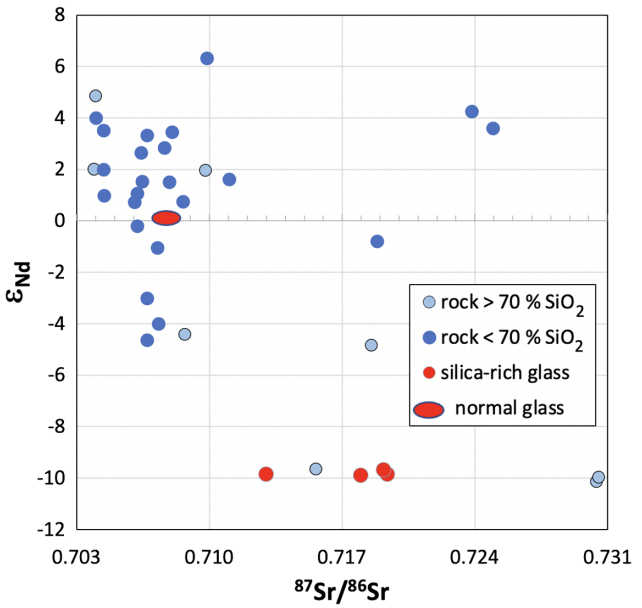

Figure 4 ε_{Nd} *versus* $^{87}Sr/^{86}Sr$ for normal atacamaite glass (red ellipse after Gattacceca *et al.*, 2021), silica-rich glass (red dots) and magmatic rocks from a two degree square centred on the main strewn-field (24–26° S, 66.5–68.5° W), extracted from Oliveros *et al.* (2020) database, cut above $SiO_2 = 60$ wt. %. Dark and light blue corresponds to rock with less or more than 70 wt. % SiO_2.

and a $^{40}Ar/^{36}Ar$ *y* intercept of 316.5 ± 9.4. Likewise, the triangular envelope defined by total fusion data is defined toward the $^{39}Ar/^{40}Ar$ *x* axis by forty data points (Fig. S-4) that define a linear array (MSWD = 1.20) with an apparent intercept age of 6.83 ± 0.69 Ma and a $^{40}Ar/^{36}Ar$ *y* intercept of 321.9 ± 4. The pooled mean age from the high silica glass of 6.87 ± 0.62 Ma, suggests an indistinguishable age for the two glass types within 0.29 ± 0.62 Ma (±2σ; Fig. 2).

Geochemistry. For detailed geochemical analysis, three silica-rich samples were selected from the western satellite strewn field (Fig. 1) and three others from different sites in the main strewn field. The six silica-rich samples are characterised by an average SiO_2 content of 85.4 ± 0.3 wt. % compared to 63.7 ± 2.9 wt. % for normal atacamaites (Table S-2). Variability (max/min −1) is below 20 % for the majority of elements including Si, Al, Fe, K, Ti, rare earths and a number of other trace elements. This points toward a rather homogeneous melt batch, including the main strewn field samples. No significant difference is observed between samples from the satellite strewn field, and silica-rich samples from the main strewn field. A trace element spidergram (Fig. 3a, Table S-4) indicates that normal atacamaites have patterns typical of the mainly dacitic local Jurassic batholith (compared to Lucassen *et al.*, 2006; Oliveros *et al.*, 2020). On the other hand, the silica-rich glass has significant depletion in Cs, Rb, Sr that cannot be accounted for by a more differentiated magma, but points toward a weathering effect. The total alkali content of 0.35 ± 0.01 wt. % is also consistent with strong weathering (Fig. S-5). We tested the hypothesis that the high silica glass derived from a mixture of 40.2 wt. % normal atacamaite and 59.8 wt. % quartz sand present as a layer covering the dacitic magmatic target (proportion matched to give equal SiO_2 content). The ratio of the real silica-rich glass to the modelled normal atacamaite + quartz mixture is shown in Figure 3b. A strong deficit of alkali elements, especially for the lighter ones, is evidenced, as well as a deficit of Co and Ni. We may thus propose that alkali depletion is due to the dissolution of feldspars while Co and Ni depletion is due to negligible extraterrestrial contamination in the silica-rich glass compared to the normal glass (see discussion in Supplementary Information). Regarding the other enriched elements, those enriched by a factor of more than 2 are Sc, Ti, Cr, Mn, Zr, Nb, Hf, Ta. This may be explained by addition of sand heavy minerals such as chromite and zircon. To summarise, the silica-rich glass could be derived by melting a weathered dacitic target of similar composition as normal atacamaite, together with quartz sand and heavy minerals.

This interpretation can be confronted with the isotopic compositions of Sr and Nd (Fig. 4, Table S-5). With an $^{87}Sr/^{86}Sr$ value of 0.713 for K260 sample and an average of 0.719 for the three samples from the satellite strewn field, the silica-rich glass is more radiogenic than the normal glass that has an $^{87}Sr/^{86}Sr$ ratio <0.708. Most local rocks have $^{87}Sr/^{86}Sr$ below 0.710, and the ones with ratios higher than 0.718 are silica-rich. The Nd isotopic ratio also shows a distinct signature for the two glasses. The isotopic data thus invalidate the simple model based on element data alone, and indicate that the magmatic component in the silica-rich glass does not have the same isotopic signature as the source of normal atacamaite.

Discussion and Conclusions

Based on indistinguishable formation ages within uncertainties, on the geochemical constraints, on the observation that both normal glass and high silica glass coexist within a single sample and the fact that chemically identical silica-rich glasses are present in both the main and the satellite strewn fields, a single impact event seems to be the most likely hypothesis. In addition, the alternative hypothesis that the two glass types were generated by two independent impacts seems to be an unlikely possibility based on a probabilistic basis. Indeed, following the model proposed by Rochette *et al.* (2023), one can compute the probability that a second impact occurred within a maximum 0.9 Ma time window (based on the uncertainties of $^{40}Ar/^{39}Ar$ ages) and within 100 km distance from the one producing the normal atacamaites. This probability is 0.4 % for a crater >1 km diameter.

Therefore, we can put forward a scenario of impact melting of the Atacama Desert surface in two stages (Fig. S-6). In the first stage, the upper metres of the target, consisting of aeolian sands and weathered regolith derived from magmatic materials (*e.g.*, tephra or transported detritus), is melted and reduced without significant impactor contamination, and ejected toward both the western satellite and the main strewn fields. Fractions of a second later an underlying unweathered dacitic rock is melted in greater quantity, mixed variably with the oxidised sprayed impactor, and ejected only in the main strewn field, *i.e.* over a shorter distance than the first batch (about 50 km less). Surface regolith cannot simply derive from the underlying dacite as isotopic data and trace element patterns do not match, but it may derive from a mixture of late tephra and/or degradation of transported local rocks. Another type of scenario is a lateral chemical and/or lithological contrast within the melted surface, *e.g.*, made of a fresh dacitic outcrop surrounded by a regolith, with synchronous melting. However, we favour the vertical layering scenario based on the principle of Occam's razor and the fact that the lateral contrast scenario does not provide a logical sequential scenario for the impactor contamination contrast. In our scenario the first melt, heated by radiating compressed air, is not interacting with the impactor spray. This scenario, compatible with theoretical impact modelling (Artemieva, 2002; Wakita *et al.*, 2022; Carlson *et al.*, 2023), also implies that the first melt batch was ejected farther than the more abundant second one. As a consequence, it is expected that the source

crater should be located closer to the main strewn field. The source crater is tentatively located along the apparent ejecta lobe oriented N120°, East of the main strewn field (Fig. 1).

Geochemically distinct types of ballistically ejected impact glasses linked to a single impact event have been described in the literature, such as around the Zhamanshin and Kamil craters (Jonasova *et al.*, 2016; Fazio *et al.*, 2016). However, the 100 km wide atacamaite strewn field is a rather unique example where the kinematics of impactor-target interaction can be traced with such detail. The second largest comparable case, the Darwin 50 km wide strewn field, does show chemical variability but not with such a dichotomy in particular in impactor contamination and redox state (Howard, 2008). The origin of the reduction observed in the silica-rich glass remains a puzzle: one could invoke biomass carbon, as advocated for the fire derived Pica glass in northern Atacama (Roperch *et al.*, 2017) and the Darwin glass (Howard *et al.*, 2013). The Libyan Desert glass strewn field is larger than the atacamaite one, but its extension is suspected to be related to fluvial transport (Jimenez-Martinez *et al.*, 2015) and it shows no evidence of ballistic transport. It is therefore not a relevant comparison.

Acknowledgements

The Ar laser probe facility was realised with the financial support of CNR. We acknowledge R. Romero, who provided eight more Si-rich samples, as well as the input of one anonymous reviewer, K. Howard and Journal editor that helped improving our manuscript. Work partly supported by the ANR ET-Megafire project (ANR-21-CE49-0014-03).

Editor: Romain Tartèse

Additional Information

Supplementary Information accompanies this letter at https://www.geochemicalperspectivesletters.org/article2418.

Cite this letter as: Rochette, P., Di Vincenzo, G., Gattacceca, J., Barrat, J.A., Devouard, B., Folco, L., Musolino, A., Quesnel, Y. (2024) A two stage impact melting process in an impact glass strewn field from the Atacama Desert. *Geochem. Persp. Let.* 30, 28–33. https://doi.org/10.7185/geochemlet.2418

References

Artemieva, N. (2002) Tektite origin in oblique impact: numerical modelling. In: Koeberl, C. Plado, J. (Eds.) *Impacts in Precambrian Shields*, Springer-Verlag, Berlin, 257–276. https://doi.org/10.1007/978-3-662-05010-1_10

Carlson, M.A., Melosh, H.J., Johnson, B.C. (2023) Atmospheric Interactions of Ejecta on Earth and Mars Including the Effect of Vaporization. *The Planetary Science Journal* 4, 194. https://doi.org/10.3847/PSJ/acf9f1

Di Vincenzo, G. (2022) High precision multi-collector $^{40}Ar/^{39}Ar$ dating of moldavites (Central European tektites) reconciles geochronological and paleomagnetic data. *Chemical Geology* 608, 121026. https://doi.org/10.1016/j.chemgeo.2022.121026

Ebert, M., Hecht, L., Deutsch, A., Kenkmann, T., Wirth, R., Berndt, J. (2014) Geochemical processes between steel projectiles and silica-rich targets in hypervelocity impact experiments. *Geochimica et Cosmochimica Acta* 135, 257–279. https://doi.org/10.1016/j.gca.2014.02.034

Fazio, A., D'Orazio, M., Cordier, C., Folco, L. (2016) Target-projectile interaction during impact melting at Kamil Crater, Egypt. *Geochimica et Cosmochimica Acta* 18, 33–50. http://dx.doi.org/10.1016/j.gca.2016.02.003

Folco, L., Carone, L., D'Orazio, M., Cordier, C., Suttle, M.D., van Ginneken, M., Masotta, M. (2022) Microscopic impactor debris at Kamil Crater (Egypt): The origin of the Fe-Ni oxide spherules. *Geochimica et Cosmochimica Acta* 335, 297–322. https://doi.org/10.1016/j.gca.2022.06.035

Folco, L., Rochette, P., D'Orazio, M., Masotta, M. (2023) The chondritic impactor origin of the Ni-rich component in Australasian tektites and microtektites. *Geochimica et Cosmochimica Acta* 360, 231–240. https://doi.org/10.1016/j.gca.2023.09.018

Gattacceca, J., Devouard, B., Barrat, J.A., Rochette, P., Balestrieri, M.L., Bigazzi, G., Ménard, G., Moustard, F., Dos Santos, E., Scorzelli, R., Valenzuela, M. (2021) A 650 km^2 Miocene strewn field of splash-form impact glasses in the Atacama Desert, Chile. *Earth and Planetary Science Letters* 569, 117049. https://doi.org/10.1016/j.epsl.2021.117049

Glass, B.P., Simonson, B.M. (2013) *Distal Impact Ejecta Layers: A Record of Large Impacts in Sedimentary Deposits*. Springer, Heidelberg. https://doi.org/10.1007/978-3-540-88262-6

Hamann, C., Fazio, A., Ebert, M., Hecht, L., Wirth, R., Folco, L., Deutsch, A., Reimold, W.U. (2018) Silicate liquid immiscibility in impact melts. *Meteoritics and Planetary Science* 53, 1594–1632. https://doi.org/10.1111/maps.12907

Howard, K.T. (2008) Geochemistry of Darwin glass and target rocks from Darwin crater, Tasmania, Australia. *Meteoritics and Planetary Science* 43, 479–496. https://doi.org/10.1111/j.1945-5100.2008.tb00667.x.

Howard, K.T., Bailey, M.J., Berhanu, D., Bland, P.A., Cressey, G., Howard, L.E., Jeynes, C., Matthewman, R., Martins, Z., Sephton, M.A., Stolojan, V., Verchovsky, S. (2013) Biomass preservation in impact melt ejecta. *Nature Geoscience* 6, 1018–1022. https://doi.org/10.1038/ngeo1996

Hutzler, A., Gattacceca, J., Rochette, P., Braucher, R., Carro, B., Christensen, E J., Cournede, C., Gounelle, M., Laridhi Ouazaa, N., Martinez, R., Valenzuela, M., Warner, M., Bourles, D. (2016) Description of a very dense meteorite collection area in western Atacama: Insight into the long-term composition of the meteorite flux to Earth. *Meteoritics and Planetary Science* 51, 468–482. https://doi.org/10.1111/maps.12607

Jimenez-Martinez, N., Ramirez, M., Diaz-Hernandez, R., Rodriguez-Gomez, G. (2015) Fluvial Transport Model from Spatial Distribution Analysis of Libyan Desert Glass Mass on the Great Sand Sea (Southwest Egypt): Clues to Primary Glass Distribution. *Geosciences* 5, 95–116. https://doi.org/10.3390/geosciences5020095

Jonášová, Š., Ackerman, L., Žák, K., Skála, R., Ďurišová, J., Deutsch, A., Magna, T. (2016) Geochemistry of impact glasses and target rocks from the Zhamanshin impact structure. *Geochimica et Cosmochimica Acta* 190, 239–264. https://doi.org/10.1016/j.gca.2016.06.031

Koeberl, C. (2014) 2.5 - The Geochemistry and Cosmochemistry of Impacts. In: Holland, H.D., Turekian, K.K. (Eds.) *Treatise on Geochemistry*. Second Edition, Elsevier, Amsterdam, 73–118. https://doi.org/10.1016/B978-0-08-095975-7.00130-3

Lucassen, F., Kramer, W., Bartsch, V., Wilke, H.-G., Franz, G., Romer, R.L., Dulski, P. (2006) Nd, Pb, and Sr isotope composition of juvenile magmatism in the Mesozoic large magmatic province of northern Chile (18–27°S): indications for a uniform subarc mantle. *Contributions to Mineralogy and Petrology* 152, 571–589. https://doi.org/10.1007/s00410-006-0119-y.

Ma, P., Aggrey, K., Tonzola, C., Schnabel, C., De Nicola, P., Herzog, G.F., Wasson, J.T., Glass, B.P., Brown, L., Tera, F., Middleton, R. (2004) Beryllium-10 in Australasian tektites: constraints on the location of the source crater. *Geochimica et Cosmochimica Acta* 68, 3883–3896. https://doi.org/10.1016/j.gca.2004.03.026

McDonough, W.F., Sun, S.-s. (1995) The composition of the Earth. *Chemical Geology* 120, 223–253. https://doi.org/10.1016/0009-2541(94)00140-4

Oliveros, V., Moreno-Yaeger, P., Flores, L. (2020) Igneous Rock Associations 25. Pre-Pliocene Andean Magmatism in Chile. *Geoscience Canada* 47, 65–82. https://doi.org/10.12789/geocanj.2020.47.158

Rochette, P., Gattacceca, J., Devouard, B., Moustard, F., Bezaeva, N.S., Cournède, C., Scaillet, B. (2015) Magnetic properties of tektites and other related impact glasses. *Earth and Planetary Science Letters* 432, 381–390. https://doi.org/10.1016/j.epsl.2015.10.030

Rochette, P., Braucher, R., Folco, L., Horng, C.S., Aumaître, G., Bourlès, D.L., Keddadouche, K. (2018) ^{10}Be in Australasian microtektites compared to

tektites: Size and geographic controls. *Geology* 46, 803–806. https://doi.org/10.1130/G45038.1

Rochette, P., Baratoux, D., Braucher, R., Cornec, J., Debaille, V., Devouard, B., Gattacceca, J., Gounelle, M., Jourdan, F., Moustard, F., Nomade, S. (2023) Linking a distal ejecta with its source crater: a probabilistic approach applied to tektites. *Comptes Rendus Geosciences* 355, 145–155. https://doi.org/10.5802/crgeos.206.

Roperch, P., Gattacceca, J., Valenzuela, M., Devouard, B., Lorand, J.P., Arriagada, C., Rochette, P., Latorre, C., Beck, P. (2017) Surface vitrification caused by natural fires in Late Pleistocene wetlands of the Atacama Desert. *Earth and Planetary Science Letters* 469, 15–26. https://doi.org/10.1016/j.epsl.2017.04.009

Wakita, S., Genda, H., Kurosawa, K., Davison, T.M., Johnson, B.C. (2022) Effect of impact velocity and angle on deformational heating and postimpact temperature. *Journal of Geophysical Research: Planets* 127, e2022JE007266. https://doi.org/10.1029/2022JE007266

Geochemical Perspectives Letters

A two-stage impact melting process in an impact glass strewn field from the Atacama Desert

P. Rochette, G. Di Vincenzo, J. Gattacceca, J.A. Barrat, B. Devouard, L. Folco, A. Musolino, Y. Quesnel

Supplementary Information

The Supplementary Information includes:

- Samples and Methods
- Estimating Extraterrestrial Contamination
- Mixture of the Silica-rich and Normal Glasses?
- Tables S-1 to S-5
- Figures S-1 to S-10
- Supplementary Information References

Samples and Methods

Magnetic susceptibility of all silica-rich glass was measured using a MFK1 bridge (Rochette *et al*., 2015). For detailed analysis, three samples were selected from the western strewn-field, two from El Medano (EM1a and EM2b) and one from Caleta el Cobre (CeC) meteorite collection areas (Hutzler *et al*., 2016), distant by 25 km (Fig. 1). Systematic investigation of samples from the main strewn-field revealed also translucent teardrop samples and three of them from different sites were included in the analytical batch. Macroscopic examples of silica-rich and normal samples are presented in Figures S-1 and S-7, respectively.

These six samples were analysed for major and trace elements by ICP-AES, ICP-OES and ICP-MS in SARM Nancy and UBO Brest. They were compared to 12 analyses reported in Gattacceca *et al*. (2021) on normal atacamaites. Isotopic ratio for Sr and Nd were determined in SARM Nancy and UBO Brest. In SARM, major element compositions were measured using an emission spectrometer ICP-OES (ICap 6500 Thermo Fischer), and trace elements by ICP-MS (Thermo Elemental X7) following the method detailed in Carignan *et al*. (2001). Typical analytical precisions were ca. 2 % for major elements and 5–8 % for trace elements. In UBO 100–150 mg of atacamaites were digested on a hot plate heated to 125 °C, using sequential mixtures of HF/HNO_3, HNO_3 and HCl. The aliquots of the obtained solutions were used for the determination of major and trace element concentrations, Sr and Nd isotopic compositions. Major elements, Ni and Co abundances were analysed by inductively coupled plasma-atomic emission spectrometry (ICP-AES) using a Horiba Jobin Yvon Ultima spectrometer and following the analytical procedure of Cotten *et al*. (1995). Relative standard deviations are <2 %. The accuracy is better than 7 % for Na and P, and much better than 3 % for the other elements. Trace element concentrations were measured with a Thermo® Element2 ICP-SFMS (inductively coupled plasma-sector field mass spectrometer). Concentrations were determined following the procedure described by Barrat *et al*. (2012, 2016). Based on results obtained on many standards, the reproducibility and accuracy are always better than 5 %. Strontium and Nd fractions were prepared following conventional ion exchange techniques. They were analysed using a Thermo® Triton TIMS (thermal ionisation mass spectrometer). Isotopic ratios were normalised against $^{86}Sr/^{88}Sr = 0.1194$ and $^{146}Nd/^{144}Nd = 0.7219$. The values obtained for NBS 987 and La Jolla standards during the course of the study are respectively $^{87}Sr/^{86}Sr = 0.710254 \pm 0.000003$ (2σ, $n = 8$) and $^{143}Nd/^{144}Nd = 0.511830 \pm 0.000003$ (2σ, $n = 6$).

Microscopic observations were performed using Hitachi S3000-N instrument scanning electronic microscope (SEM) in backscattered mode operated at 15 kV, equipped with a Bruker energy dispersive spectrometry (EDS) microanalysis system. Microanalyses were obtained by electron microprobe analysis using a CAMECA SX-100 at the Centre de Microanalyse de Paris VI (CAMPARIS). The operating conditions were 15 kV accelerating voltage with a current of 15 nA and a defocused beam of 10 µm. Both natural and synthetic standards were used for calibration: albite for Na; anorthite for Al; apatite for P; wollastonite for Si, Ca; orthoclase for K; pyrite for S; $MnTiO_3$ for Mn and Ti; fayalite for Fe; forsterite for Mg, and NiO for Ni. The detection limits were 723 µg g^{-1} for K, 684 µg g^{-1} for Ca, 499 µg g^{-1} for Al, 959 µg g^{-1} for Na, 639 µg g^{-1} for Si, 544 µg g^{-1} for Mg, 494 µg g^{-1} for P, 767 µg g^{-1} for Mn, 384 µg g^{-1} for Ni, 797 µg g^{-1} for Fe, and 795 µg g^{-1} for Ti.

$^{40}Ar/^{39}Ar$ analyses were performed at IGG–CNR (Pisa, Italy) on three samples from the normal glass (samples K51, K48G, K326) and one sample (EM1a) from the silica-rich type. Glass samples were crushed and sieved, and glass separates were recovered from the 0.35–0.50 mm grain size. $^{40}Ar/^{39}Ar$ analyses were performed using both the laser step-heating and the laser total fusion techniques. Glass separates, after final cleaning by alternating methanol and deionised water, were wrapped in Al foil and irradiated along with the Alder Creek sanidine (ACs) in the core of the TRIGA reactor at the Università di Pavia (Italy) in three distinct batches for three hours (Table S-3): 1) irradiation PAV-87, May 2021; 2) irradiation PAV-88, March 2022; 3) irradiation PAV-89, October 2022. Argon isotope compositions were determined using either a single-collector noble gas mass spectrometer (irradiation PAV-88 and only step-heating analysis) or a multi-collector mass spectrometer (irradiation PAV-87 and PAV-88). The neutron fluence was monitored by analysing single grains of the ACs, which were melted using a continuous wave CO_2 laser (New Wave Research MIR10– 30 CO_2 laser system). Laser step-heating and total fusion experiments of glass separates were performed using either (see Table S-3) a fiber laser (RedEnergy G4 50W EP-Z, SPI Lasers, 1059–1065 nm) or the same CO_2 laser as above. The laser beams were defocused to 2-mm spot size and slowly rastered over the glass separate. Steps were carried out at increasing laser power until complete melting. Argon isotope compositions determined through the single-collector noble gas mass spectrometry were acquired by peak jumping using a MAP215-50 (Mass Analyser Products) mass spectrometer, fitted with a secondary electron multiplier. Gas purification (10 min, including ~2 min of lasering) was achieved by one SAES C-50 getter held at 400 °C and one Saes CapaciTorr HV200 getter held at room temperature. Blanks were analysed every three to four analyses. A polynomial function was fit to blanks analysed during the day of acquisition, and unknown analyses were corrected based on the time of measurement. Line blank variation is given in the Table S-3. More details about mass spectrometer analysis can be found in Di Vincenzo and Skála (2009). Argon isotope compositions determined through the multi-collector noble gas mass spectrometry were acquired simultaneously using an ARGUS VI (Thermo Fisher Scientific) mass spectrometer. Ar isotopes from 40 to 37 were acquired using Faraday detectors, equipped with 10^{12} Ω resistors for ^{40}Ar and 10^{13} Ω resistors for ^{39}Ar, ^{38}Ar and ^{37}Ar. Faraday detectors were cross calibrated for the slight offset using air shots. Before the acquisition of data from irradiation PAV-88, the mass spectrometer was upgraded with an additional amplifier equipped with a 10^{13} Ω resistor on cup H1 (^{40}Ar). ^{36}Ar was measured using a Compact Discrete Dynode (CDD) detector. Gas purification (4 min, including ~1 min of lasering) was achieved using three SAES NP10 getters (one water cooled, held at ~400 C and two at room temperature). Blanks were generally monitored every two runs and were subtracted from succeeding sample results. Line blanks are given in the Table S-2. More details about mass spectrometer calibration and analysis can be found in Di Vincenzo *et al*. (2021). The correction factors for interfering isotopes from K and Ca were determined on K-rich and Ca-rich glasses and are listed in Table S-3. Ages were calculated using decay constants recalculated by Min *et al*. (2000), an atmospheric $^{40}Ar/^{36}Ar$ ratio of 298.56 ± 0.31 (Lee *et al*., 2006), and an age of 1.1848 ± 0.0012 Ma for the ACs reference mineral (Niespolo *et al*., 2017). Data corrected for post-irradiation decay, mass discrimination effects and blanks (relative abundances) are listed in Table S-3. Uncertainties on single runs are 2σ analytical uncertainties, including in-run statistics and uncertainties in the discrimination factor, interference corrections and procedural blanks. Uncertainties on the total gas ages and on error-weighted means also include the uncertainty on the fluence monitor (2σ internal errors). The full uncertainty given for the mean age from normal glass also include systematic uncertainties (on the age of the reference material and on ^{40}K total decay constant). Repeated analyses of individual fragments of moldavite VLTA2242 (Di Vincenzo, 2022) were used for accuracy control of the acquired $^{40}Ar/^{39}Ar$ data. Data relative to irradiation PAV-87 are reported in Di Vincenzo (2022), those relative to irradiations PAV-88 and PAV-89 are listed in Table S-3. Data for three different stack positions from irradiation PAV-88 and PAV-89 yielded a pooled mean age of 14.7520 ± 0.0098 Ma (Table S-3), which is indistinguishable at 1σ level from the value (14.7495 ± 0.0045 Ma) reported in Di Vincenzo (2022). The mean age of 6.578 ± 0.011 Ma (±0.013 Ma including all sources of errors) reported in the main text for the

normal glass has been calculated using the pooled R-value (Atacamaite/ACs) of 5.560 ± 0.010 (± 2σ, MSWD = 0.63, Probability 0.75), derived from intra-sample concordant $^{40}Ar/^{39}Ar$ data from step-heating and total fusion data, and using equations and error propagation given in Renne *et al*. (1998). The R-value provides a useful means for allowing a direct comparison of a reference material and an unknown sample regardless of the assumed age (see Karner and Renne, 1998), and consists of the ratio between the $^{40}Ar^*/^{39}Ar_K$ ratios of two co-irradiated samples. The R-value reported here can be therefore used in the future to update the age of the atacamaites whenever the age of the ACs reference material is refined.

Estimating Extraterrestrial Contamination

In Gattacceca *et al*. (2021), the Co and Ni *versus* Fe correlations shown by normal atacamaites were used to estimate a metallic impactor composition with Ni and Co contents of 5.4 and 0.45 wt. %, respectively. We provide in Figure S-8 a mixing curve between this model impactor and a model rock containing 19.2 ppm Ni and 10 ppm Co. This model composition was derived from the average Ni content of the model andesite derived from Oliveros *et al*. (2020) and the Co content providing the best fit for the Si-rich glass.

The model confirms that normal atacamaites except one sample (PT7e, see discussion below) show contamination varying from 3 to 9 %. On the other hand, it points toward a 0.1 to 0.2 % of contamination for the silica-rich samples. However, this estimate is an upper bound as there is a strong possibility of enrichment in the silica-rich target material by Ni and Co unrelated to the impactor. It could be due to accumulation of micrometeorites on the surface. Indeed, the surface of the Atacama Desert is a good accumulator for micrometeorites due to its very old age (van Ginneken *et al*., 2017). Moreover, the heavy mineral enrichment invoked for explaining the enrichment in *e.g.*, Ti, Cr, Zr of Figure 3b, could also have enriched the target in Ni and Co. Therefore, we can safely state that 0.1–0.2 % is the upper bound of impactor contamination in the silica-rich glass in these 6 samples. A significant contamination by an iron impactor should also be seen on the magnetic susceptibility data, which is available on 124 samples. A 2 % impactor contamination should result in a Fe_2O_3 content increasing from 4.64 to 7.5 wt. %. This would result in a strong change of susceptibility even if all iron is kept paramagnetic (77 to 128 × 10^{-9} m^3/kg). Only one out of 124 samples showed anomalously high susceptibility due to insertion of a normal atacamaite droplet. So, we can conclude that less than a percent of high silica glass may show significant impactor contamination (*i.e.* >1 %).

Mixture of the Silica-rich and Normal Glasses?

The homogeneity of chemical composition of the six silica-rich studied sample also precludes a significant mixing with normal atacamaite. Among 124 silica-rich samples, identified by their translucent character, only one had a diverging magnetic susceptibility (K260m), the others being well grouped around the mean susceptibility value. This indicates a rather constant iron amount (see Fig. S-3). Mixing in equal proportion the two melt batches (with average susceptibilities of 77 and 191 × 10^{-9} m^3/kg, respectively) would result in an increase of magnetic susceptibility of a factor 1.7 (at least, *i.e.* without ferromagnetic contribution). It should also show visually during the translucency test. Therefore, we can conclude that composite samples with significant inclusion of normal atacamaite constitute at most 1 % of the collection.

K260M sample is a unique case where we identified a millimetric droplet of magnetite-rich normal atacamaite, inserted in a hole of a silica-rich sample from the main strewn field. Such a find indicates that the two particles, present independently in the impact plume, were welded together before cooling, thus likely in flight. This apparently contradicts our two-stage scheme (Fig. S-6) with the normal atacamaite being launched after the silica-rich material. However, it is possible to invoke a combination of trajectories allowing these two particles to encounter during the descending flight of the silica-rich particle (Fig. S-9).

Now, what if full mixture of the two melts remained undetected in the normal atacamaite collection? In particular, could the weakly contaminated PT7e sample represent such a mixture (as suggested in Fig. S-8)? The chemical composition of PT7e clearly excludes this hypothesis based on the lack of alkali depletion, typical of silica-rich material (compare Fig. S-10 and Fig. 3b). The fit between PT7e and normal atacamaite, apart on Ni and Co, clearly point toward PT7e being fully derived from the same target material but with a much lower extra-terrestrial contamination (about 0.7 %).

Supplementary Tables

Table S-1 Results of electron probe microanalyses (EPMA) for 5 transparent atacamaites (in wt. %) and the composite sample K260M (Fig. S-1d).

Sample	SiO_2	Al_2O_3	TiO_2	FeO	MnO	MgO	CaO	Na_2O	K_2O	NiO	total
K260-46	87.16	0.45	7.23	3.82	bdl	1.13	0.15	bdl	0.28	bdl	100.34
	86.67	0.57	7.40	3.89	bdl	0.98	0.16	bdl	0.29	bdl	100.07
	85.85	0.51	7.92	4.04	bdl	0.79	0.10	bdl	0.31	bdl	99.61
	87.44	0.46	7.53	3.82	bdl	0.82	0.19	bdl	0.30	bdl	100.67
K260-49	85.60	0.64	8.19	4.40	0.09	0.68	0.11	bdl	0.33	bdl	100.11
	85.45	0.58	8.69	4.16	0.10	0.70	0.10	bdl	0.30	bdl	100.16
	85.63	0.50	8.58	4.21	0.08	0.79	0.13	bdl	0.31	bdl	100.32
	85.31	0.60	8.39	4.05	0.10	0.82	0.00	bdl	0.34	bdl	99.66
K260-59	85.41	0.50	8.72	3.98	bdl	0.67	0.10	bdl	0.29	bdl	99.77
	85.96	0.52	8.33	4.36	bdl	0.70	0.10	bdl	0.28	bdl	100.38
	85.96	0.68	8.47	3.96	bdl	0.76	0.14	bdl	0.26	bdl	100.37
	84.92	0.61	8.57	4.28	bdl	0.73	0.07	bdl	0.24	bdl	99.53
K526-3	84.88	0.52	8.29	4.24	bdl	0.87	0.15	bdl	0.32	bdl	99.34
EM1a	85.48	0.54	8.26	4.25	0.11	0.91	0.09	bdl	0.27	bdl	99.98
mean	85.84	0.55	8.18	4.10	bdl	0.81	0.11	bdl	0.29	bdl	100.02
s.d.	0.74	0.06	0.47	0.19		0.12	0.05		0.03		0.38
Detection limit	0.06	0.05	0.08	0.08	0.08	0.05	.07	0.09	0.07	0.04	
composite sample											
K260M normal inclusion	60.13	0.37	12.17	11.18	0.06	1.28	5.11	3.04	2.75	0.53	96.65
K260M high-silica	84.84	0.71	7.99	4.05	0.06	0.77	0.10	0.05	0.25	bdl	98.85

Table S-2 Major element abundances (in wt. %) measured by ICP-OES (or ICP-MS for K301 and K272). Average value for normal atacamaites after Gattacceca *et al.* (2021). See main text and Figure 4 for model ratio. Rock composition reported from Oliveros *et al.* (2020) and selected within a two degrees square centered on the main strewn-field (24–26° S, 66.5–68.5° W). Rock 1: average of 4 analyses of the coastal batholith with SiO_2 within 61–64 wt. % and isotopic data similar to those of normal atacamaites. Rock 2: coastal batholith analysis with high SiO_2 content.

	CeC	EM1A	EM2B	K301	K527-37	K260-34	mean	s.d.	Normal atacamaite	model ratio	Rock1	Rock2
SiO_2	85.75	85.44	85.08			85.37	85.41	0.28	63.71	1.00	62.06	84.96
Al_2O_3	8.41	7.88	7.16			7.80	7.81	0.51	13.10	1.48	15.13	7.56
Fe_2O_3	4.74	4.83	4.25			4.72	4.64	0.26	9.78	1.18	6.18	1.10
MnO	0.059	0.059	0.085	0.072	0.071	0.071	0.07	0.01	0.08	2.16	0.11	0.02
MgO	0.84	0.99	1.44			1.03	1.07	0.26	1.92	1.39	2.97	0.54
CaO	0.15	0.17	0.32			0.19	0.21	0.07	4.62	0.11	5.64	0.28
Na_2O	0.04	0.06	0.05			0.05	0.05	0.01	3.56	0.03	3.83	2.45
K_2O	0.28	0.29	0.29	0.27	0.28	0.30	0.29	0.01	2.98	0.24	2.59	1.41
TiO_2	0.57	0.54	0.54	0.56	0.55	0.55	0.55	0.01	0.53	2.58	0.98	0.28
LOI	−0.76	−0.11	−0.32			0.20	−0.25	0.40				
total	100.08	100.15	98.89			100.28	99.85	0.65				

Table S-3 ^{40}Ar-^{39}Ar total fusion and step-heating data on impact glasses from the Atacama Desert (Chile) and moldavite VLTA2242 (for accuracy control).

Table S-3 is available for download (.xlsx) from the online version of this article at http://doi.org/10.7185/geochemlet.2418.

Table S-4 Trace element abundances (μg g^{-1}) determined by ICPMS. Rock composition reported from Oliveros *et al*. (2020) and selected within a two degrees square centered on the main strewn-field (24–26° S, 66.5–68.5° W). Rock 1: average of 4 analyses of the coastal batholith with SiO_2 within 61–64 wt. % and isotopic data similar to those of normal atacamaites. Rock 2: coastal batholith analysis with high SiO_2 contents.

	CeC	TEM1A	TEM2B	K301	K527-37	K260-34	mean	s.d.	Normal atacamaite	model ratio	Rock1	Rock2
Li				8.81	8.67		**8.74**	0.10	51.1	0.43		
Be	0.55	0.55	0.57	0.54	0.62	0.57	**0.57**	0.03	2.03	0.69		
Sc	9.38	8.97	8.46	9.49	9.05	8.94	**9.05**	0.37	9.76	2.31	17	<5
V	43.89	51.96	32.52	52.70	55.40	54.74	**48.54**	8.87	83.3	1.45	147	14
Cr	96.51	126.75	92.53	98.05	101.79	134.79	**108.40**	17.76	30.5	8.84	45.7	16
Co	14.51	17.26	15.91	16.67	15.93	18.30	**16.43**	1.30	217	0.19		
Ni	79.08	121.29	75.52	98.29	97.23	131.62	**100.50**	22.36	2556	0.10	19.3	<10
Rb	14.73	15.41	14.92	15.84	15.65	15.78	**15.39**	0.47	96.4	0.40	122	47.2
Sr	24.35	26.84	31.08	37.99	34.05	60.51	**35.80**	13.05	231.3	0.38	235	61
Y	16.23	15.90	15.85	19.03	18.74	16.24	**17.00**	1.47	39	1.08	31.7	20
Zr	203.40	197.06	214.94	224.49	220.77	203.85	**210.75**	10.92	179.7	2.92	368	269
Nb	8.75	8.58	8.60	10.38	10.17	8.80	**9.22**	0.83	11.2	2.05	10.25	7
Cs	2.61	2.77	2.38	1.51	1.66	2.80	**2.29**	0.57	5.7	1.00	5.44	0.87
Ba	162.47	160.41	218.98	209.81	196.59	231.20	**196.58**	29.49	634	0.77	271	196
La	23.59	22.80	22.18	26.09	25.24	24.40	**24.05**	1.48	37.6	1.59	18.3	5.73
Ce	42.27	40.11	38.97	47.55	46.50	42.29	**42.95**	3.42	72.1	1.48	45.75	20.13
Pr	5.48	5.26	5.28	6.14	5.95	5.62	**5.62**	0.36	8.5	1.64	6.11	2.56
Nd	20.66	19.79	20.03	22.92	22.43	21.18	**21.17**	1.27	33.2	1.59	25.44	10.38
Sm	3.89	3.80	3.85	4.26	4.18	4.09	**4.01**	0.19	6.8	1.46	5.71	2.36
Eu	0.84	0.80	0.83	0.90	0.89	0.87	**0.85**	0.04	1.1	1.96	1.18	0.4
Gd	3.31	3.17	3.17	3.55	3.48	3.29	**3.33**	0.16	6.3	1.31	5.51	2.41
Tb	0.51	0.49	0.49	0.55	0.55	0.51	**0.51**	0.03	1.0	1.29	0.86	0.43
Dy	3.05	2.94	2.97	3.19	3.20	3.05	**3.07**	0.11	6.0	1.27	5.28	2.84
Ho	0.63	0.61	0.61	0.66	0.65	0.63	**0.63**	0.02	1.2	1.26	1.07	0.59
Er	1.73	1.65	1.65	1.87	1.88	1.72	**1.75**	0.10	3.6	1.21	3.08	1.67
Yb	1.77	1.73	1.68	1.91	1.88	1.75	**1.79**	0.09	3.5	1.25	2.82	1.54
Lu	0.27	0.26	0.26	0.27	0.28	0.27	**0.27**	0.01	0.55	1.21	0.42	0.21
Hf	5.46	5.28	5.59	6.06	5.97	5.44	**5.63**	0.31	5.3	2.64	9.25	8
Ta	0.81	0.78	0.78	0.74	0.76	0.81	**0.78**	0.03	0.93	2.08		
Pb	1.05	3.60	1.22	1.89	1.77	3.85	**2.23**	1.20	2.3	2.41		
Th	6.81	6.54	6.05	7.60	7.52	6.74	**6.88**	0.59	11.6	1.47	13.76	5.56
U	0.71	0.84	0.47	0.82	0.93	0.97	**0.79**	0.18	1.8	1.09	2.91	1

Table S-5 Sr and Nd isotopic data table. Uncertainties (2σ) on $^{87}Sr/^{86}Sr$ and $^{143}Nd/^{144}Nd$ ratios are 0.000006 and 0.000004, respectively. Rock 1 and 2 after Oliveros *et al*. (2020). Average for normal atacamaite (SA) after Gattacceca *et al*. (2021).

	$^{87}Sr/^{86}Sr$	εNd	$^{143}Nd/^{144}Nd$
CeC	0.719403	−9.9	0.512133
K260	0.713003	−9.7	0.512142
TEM1A	0.719189	−9.9	0.512130
TEM2B	0.717991	−9.9	0.512132
SA	0.7078	+0.1	
Rock 1	0.7079	+1.5	0.51272
Rock 2	0.7156	−9.7	0.51214

Supplementary Figures

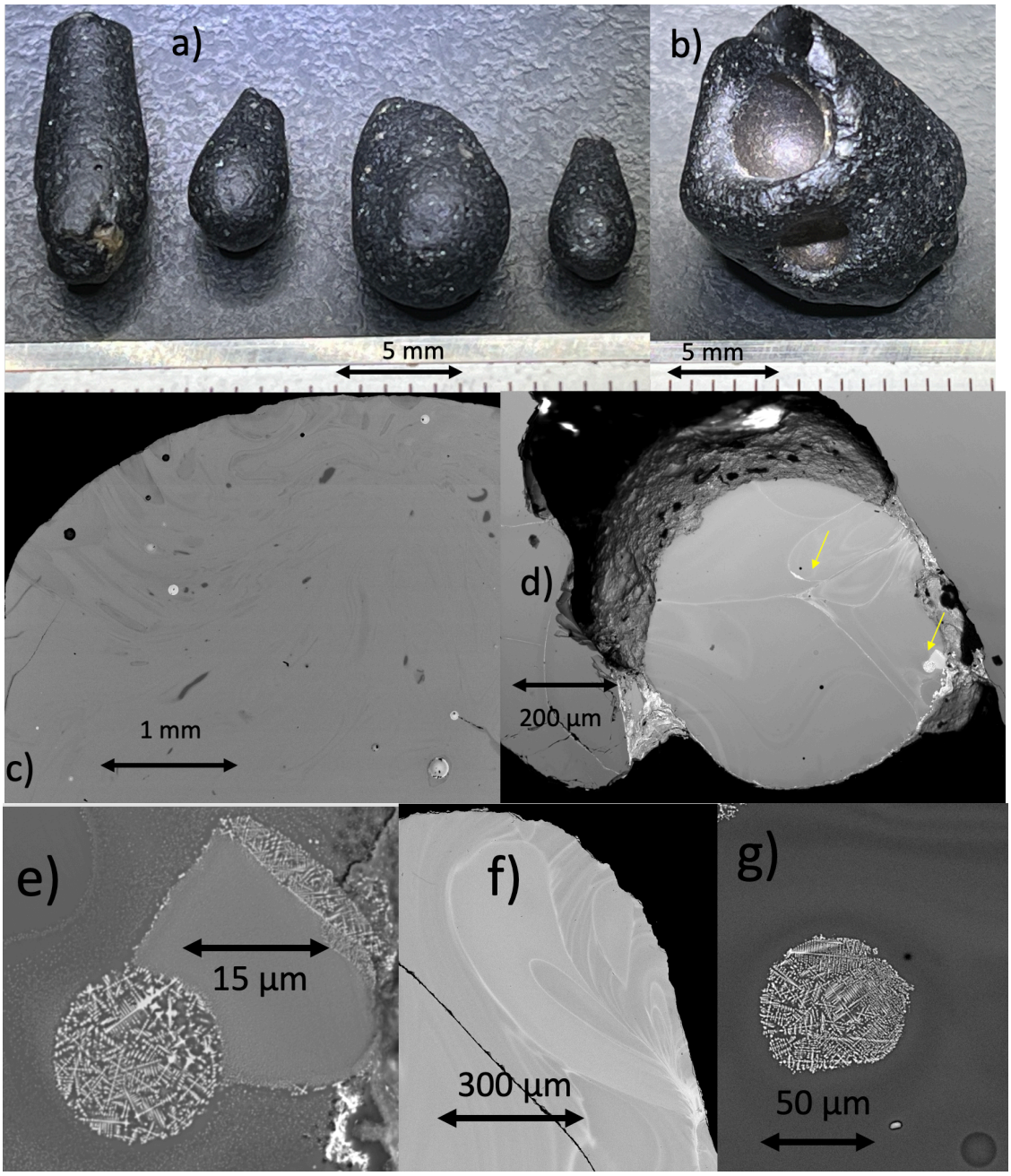

Figure S-1 Examples of full silica-rich samples with a millimetric scale: **(a)** tear drops from EM site and **(b)** largest sample from the main field (K258); backscattered SEM images of **(c)** EM1a sample (field of view is 4 mm) and **(d)** composite sample K260m. Note the average heavier element composition in the spherule enclosed within the darker silica rich sample, as well as bands rich in Fe and Ni within the spherule (left arrow). **(e)** Details of the Ni,Fe rich spherule in **(d)** (right arrow); **(f)** and **(g)** Fe- rich banding and a Fe,Ni rich spherule within normal atacamaites.

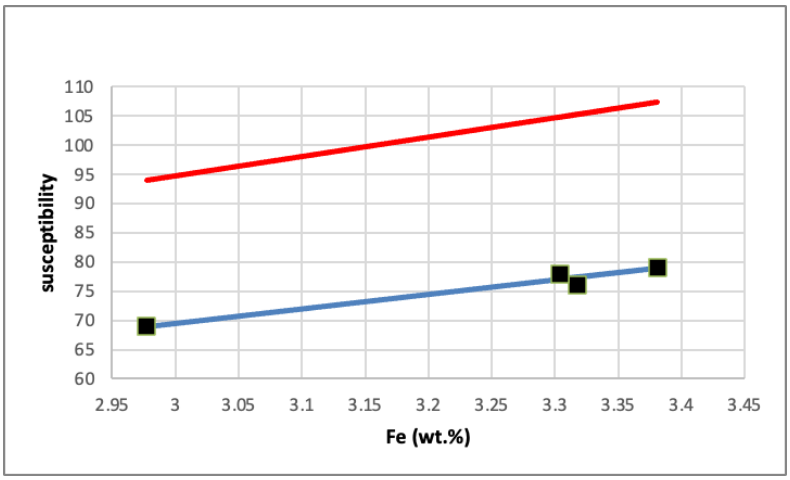

Figure S-2 Magnetic susceptibility (in 10^{-9} m^3/kg) *versus* elemental iron abundance for the analysed silica rich glasses. Data (squares) compared to modelled paramagnetic susceptibilities for Fe^{2+} (blue) and Fe^{3+} (red), after Rochette *et al.* (2015).

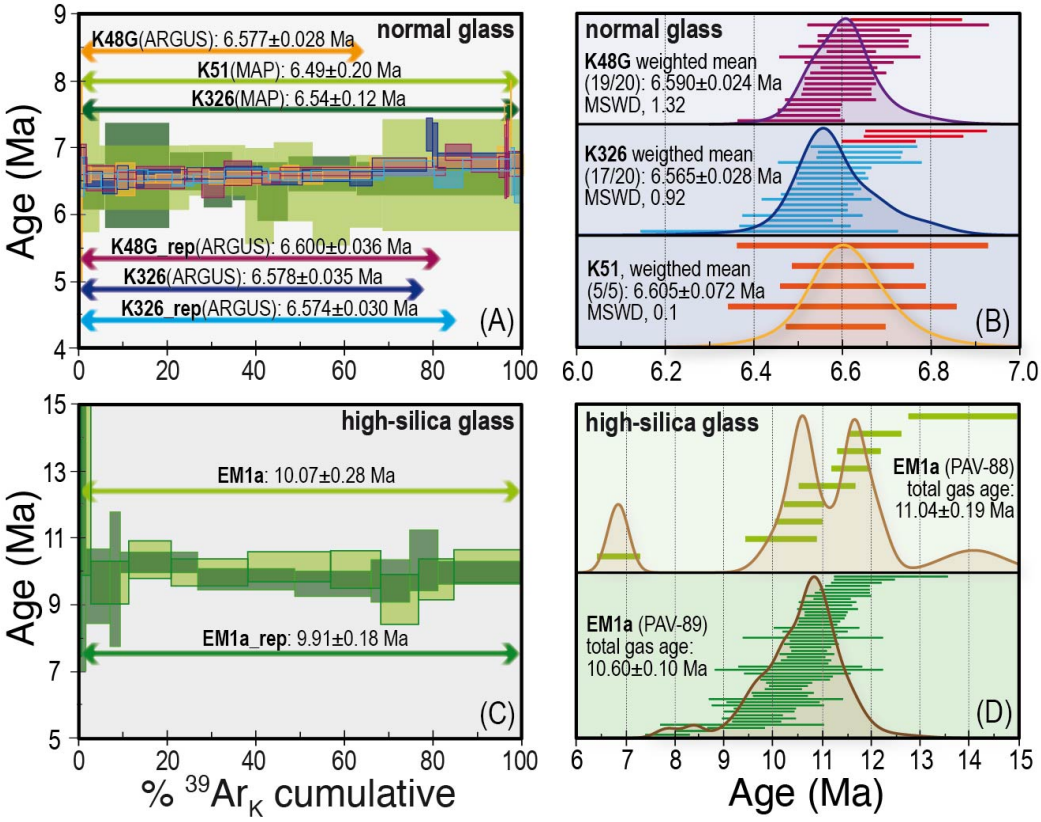

Figure S-3 **(a–c)** age spectra from step-heating experiments of normal **(a)** and high-silica glasses **(c)**. Age spectra in **(a)** affected by larger uncertainties were completed through the single-collector noble gas mass spectrometer (see Methods and Table S-3). **(b–d)** Cumulative probability and ranked distribution of $^{40}Ar/^{39}Ar$ apparent dates of normal **(b)** and high-silica **(d)** glass fragments from total fusion experiments. Data were collected from 1 to 6 fragments from the 0.35–0.50 mm grain size. Uncertainties on single runs are 2σ analytical errors. Uncertainties on the error-weighted means of total gas dates also include the uncertainty on the fluence monitor (2σ internal errors).

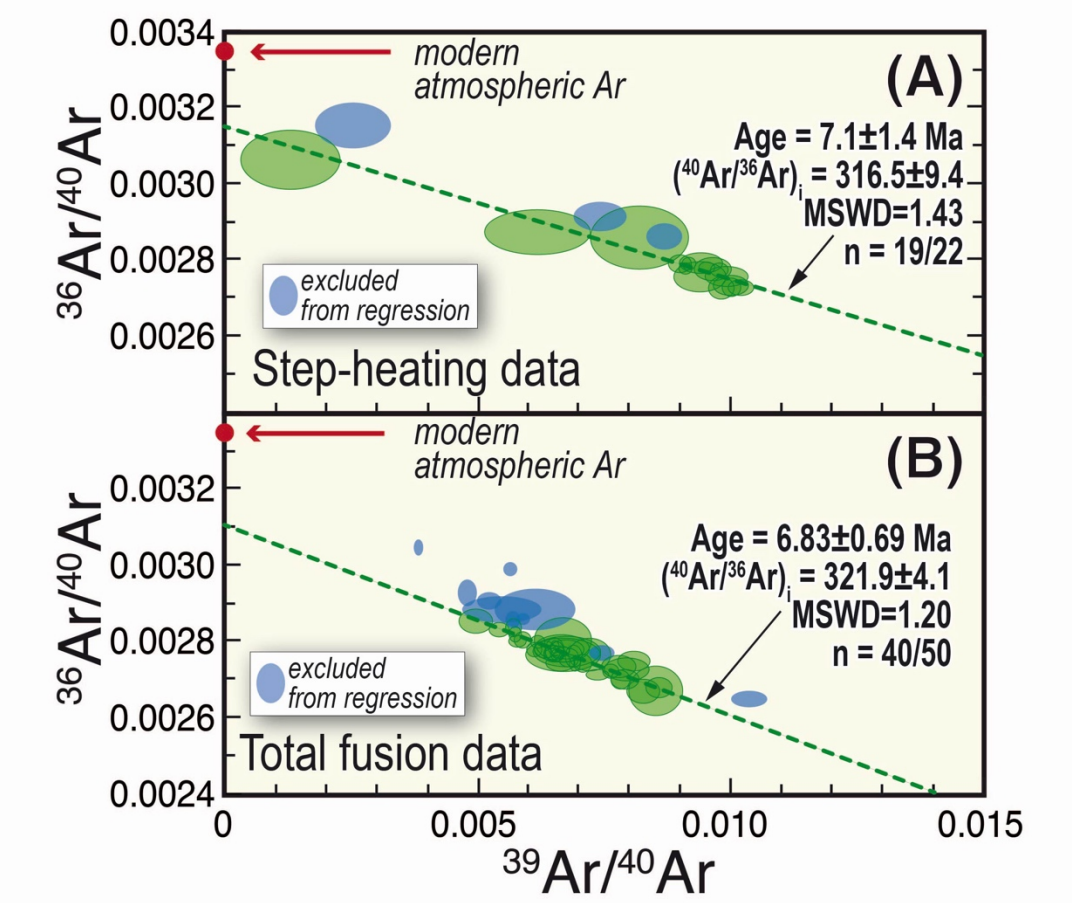

Figure S-4 Isochron plots (three-isotope correlation diagram, $^{36}Ar/^{40}Ar$ *versus* $^{39}Ar/^{40}Ar$) for **(a)** step-heating and **(b)** total fusion data of the high-silica glass sample EM1a. See main text for details. Step-heating and total fusion data define a triangular envelop that requires at least three distinct Ar components: (1) atmospheric Ar; (2) a radiogenic Ar component with dates of ~6.5–7 Ma; and (3) extraneous Ar with a $^{40}Ar/^{36}Ar$ ratio of ~320.

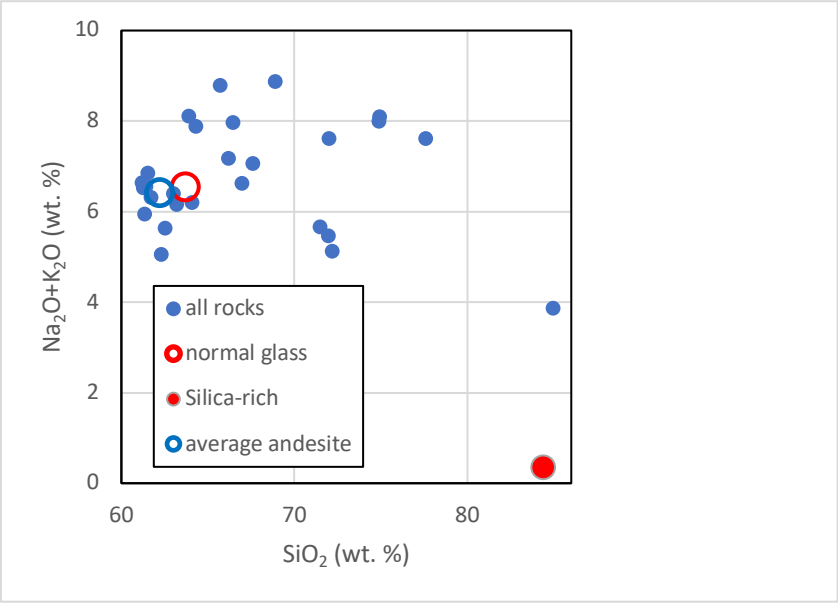

Figure S-5 TAS diagram (K_2O + Na_2O *versus* SiO_2) for average silica-rich glass (closed red circle), normal atacamaite (open red circle) and coastal batholith with SiO_2 in the 61–64 wt. % SiO_2 range and Sr, Nd isotopic ratio close to the one of normal atacamaite (data used for Fig. 3a). Small closed blue circles are all individual data from Oliveros *et al*. (2020) within a two degrees square centered on the main strewn-field (24–26° S, 66.5–68.5° W), cut above SiO_2 = 60 wt. %.

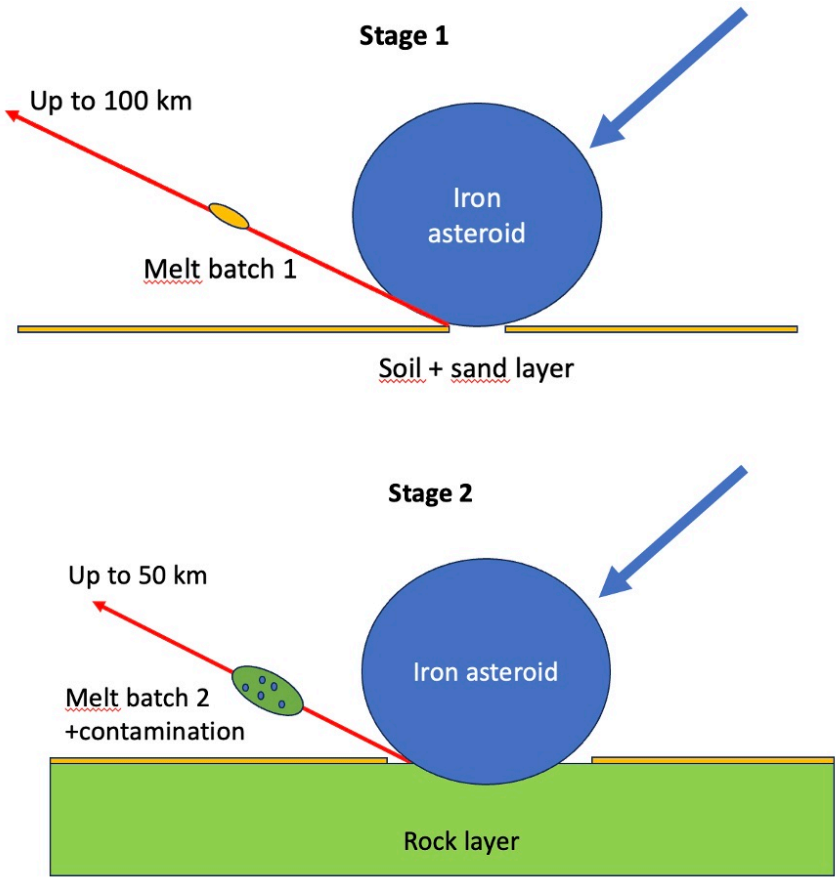

Figure S-6 Sketch of our model for two stage impact melting and ejecta.

Figure S-7 Macroscopic images of normal atacamaites: **(a)** three pieces *in situ*; **(b)** assortment of typical splash form shapes.

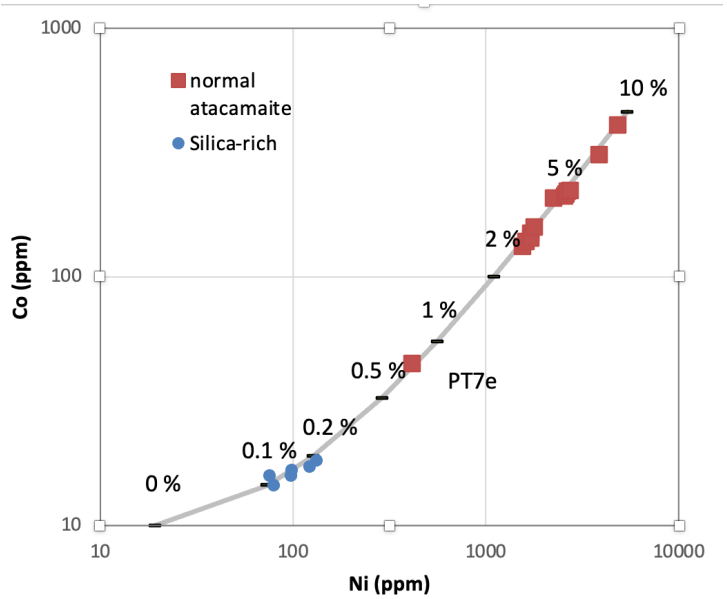

Figure S-8 Co *versus* Ni content of atacamaites superposed on a mixing model between impactor and fresh andesite.

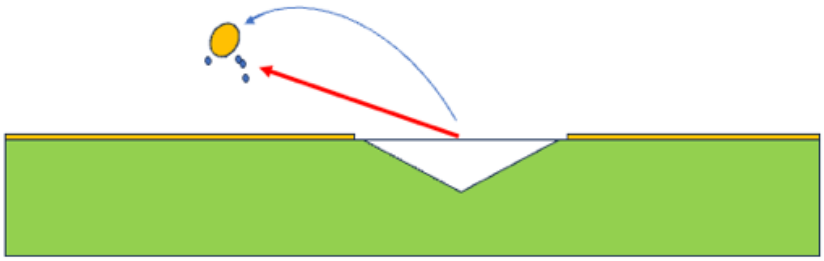

Figure S-9 Conceptual sketch explaining how K260m composite sample formed (yellow first launched silica-rich centimetric particle; blue secondary normal glass millimetric particles; based on Fig. 11 of Carlson *et al*., 2023).

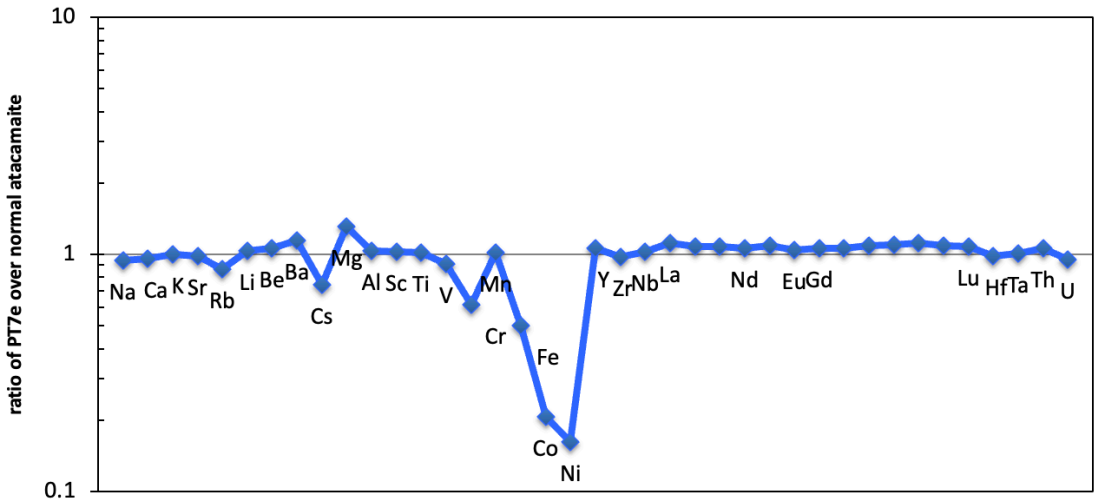

Figure S-10 Plot of PT7e sample normalised to average normal atacamaite (PT7e was not used to compute this average), following the same element ordering as Figure 3b.

Supplementary Information References

Barrat, J.A., Zanda, B., Moynier, F., Bollinger, C., Liorzou, C., Bayon, G. (2012) Geo-chemistry of CI chondrites: Major and trace elements, and Cu and Zn isotopes. *Geochimica et Cosmochimica Acta* 83, 79–92. https://doi.org/10.1016/j.gca.2011.12.011

Barrat, J.A., Dauphas, N., Gillet, P., Bollinger, C., Etoubleau, J., Bischoff, A., Yamaguchi, A. (2016) Evidence from Tm anomalies for non-CI refractory lithophile element proportions in terrestrial planets and achondrites. *Geochimica et Cosmochimica Acta* 176, 1–17. https://doi.org/10.1016/j.gca.2015.12.004

Carignan, J., Hild, P., Mevelle, G., Morel, J., Yeghicheyan, D. (2001) Routine Analyses of Trace Elements in Geological Samples using Flow Injection and Low Pressure On-Line Liquid Chromatography Coupled to ICP-MS: A Study of Geochemical Reference Materials BR, DR-N, UB-N, AN-G and GH. *Geostandards Newsletter* 25, 187–198. https://doi.org/10.1111/j.1751-908X.2001.tb00595.x

Carlson, M.A., Melosh, H.J., Johnson, B.C. (2023) Atmospheric Interactions of Ejecta on Earth and Mars Including the Effect of Vaporization. *The Planetary Science Journal* 4, 194. https://doi.org/10.3847/PSJ/acf9f1

Cotten, J., Le Dez, A., Bau, M., Caroff, M., Maury, R.C., Dulski, P., Fourcade, S., Bohn, M., Brousse, R. (1995) Origin of anomalous rare-earth element and yttrium enrichments in subaerially exposed basalts: Evidence from French Polynesia. *Chemical Geology* 119, 115–138. https://doi.org/10.1016/0009-2541(94)00102-E

Di Vincenzo, G. (2022) High precision multi-collector $^{40}Ar/^{39}Ar$ dating of moldavites (Central European tektites) reconciles geochronological and paleomagnetic data. *Chemical Geology* 608, 121026. https://doi.org/10.1016/j.chemgeo.2022.121026

Di Vincenzo, G., Skála, R. (2009) $^{40}Ar–^{39}Ar$ laser dating of tektites from the Cheb Basin (Czech Republic): Evidence for coevality with moldavites and influence of the dating standard on the age of the Ries impact. *Geochimica et Cosmochimica Acta* 73, 493–513. https://doi.org/10.1016/j.gca.2008.10.002

Di Vincenzo, G., Folco, L., Suttle, M.D., Brase, L., Harvey, R.P. (2021) Multi-collector $^{40}Ar/^{39}Ar$ dating of microtektites from Transantarctic Mountains (Antarctica): A definitive link with the Australasian tektite/microtektite strewn field. *Geochimica et Cosmochimica Acta* 298, 112–130. https://doi.org/10.1016/j.gca.2021.01.046

Gattacceca, J., Devouard, B., Barrat, J.-A., Rochette, P., Balestrieri, M.L., *et al*. (2021) A 650 km^2 Miocene strewnfield of splash-form impact glasses in the Atacama Desert, Chile. *Earth and Planetary Science Letters* 569, 117049. https://doi.org/10.1016/j.epsl.2021.117049

Hutzler, A., Gattacceca, J., Rochette, P., Braucher, R., Carro, B., Christensen, E.J., Cournede, C., Gounelle, M., Laridhi Ouazaa, N., Martinez, R., Valenzuela, M., Warner, M., Bourles, D. (2016) Description of a very dense meteorite collection area in western Atacama: Insight into the long-term composition of the meteorite flux to Earth. *Meteoritics and Planetary Science* 51, 468–482. https://doi.org/10.1111/maps.12607

Karner, D.B., Renne, P.R. (1998) $^{40}Ar/^{39}Ar$ geochronology of Roman volcanic province tephra in the Tiber River valley: Age calibration of middle Pleistocene sea-level changes. *GSA Bulletin* 110, 740–747. https://doi.org/10.1130/0016-7606(1998)110<0740:AAGORV>2.3.CO;2

Lee, J.-Y., Marti, K., Severinghaus, J.P., Kawamura, K., Yoo, H.-S., Lee, J.B., Kim, J.S. (2006) A redetermination of the isotopic abundances of atmospheric Ar. *Geochimica et Cosmochimica Acta* 70, 4507–4512. https://doi.org/10.1016/j.gca.2006.06.1563

Min, K., Mundil, R., Renne, P.R., Ludwig, K.R. (2000) A test for systematic errors in $^{40}Ar/^{39}Ar$ geochronology through comparison with U/Pb analysis of a 1.1-Ga rhyolite. *Geochimica et Cosmochimica Acta* 64, 73–98. https://doi.org/10.1016/S0016-7037(99)00204-5

Niespolo, E.M., Rutte, D., Deino, A.L., Renne, P.R. (2017) Intercalibration and age of the Alder Creek sanidine $^{40}Ar/^{39}Ar$ standard. *Quaternary Geochronology* 39, 205–213. https://doi.org/10.1016/j.quageo.2016.09.004

Oliveros, V., Moreno-Yaeger, P. Flores, L. (2020) Igneous Rock Associations 25. Pre-Pliocene Andean Magmatism in Chile. *Geoscience Canada* 47, 65–82. https://doi.org/10.12789/geocanj.2020.47.158

Renne, P.R., Swisher, C.C., Deino, A.L., Karner, D.B., Owens, T.L., DePaolo, D.J. (1998) Intercalibration of standards, absolute ages and uncertainties in $^{40}Ar/^{39}Ar$ dating. *Chemical Geology* 145, 117–152. https://doi.org/10.1016/S0009-2541(97)00159-9

Rochette, P., Gattacceca, J., Devouard, B., Moustard, F., Bezaeva, N.S., Cournède, C., Scaillet, B. (2015) Magnetic properties of tektites and other related impact glasses. *Earth and Planetary Science Letters* 432, 381–390. https://doi.org/10.1016/j.epsl.2015.10.030

van Ginneken, M., Gattacceca, J., Rochette, P., Sonzogni, C., Alexandre, A., Vidal, V., Genge, M. J. (2017) The parent body controls on cosmic spherule texture: Evidence from the oxygen isotopic compositions of large micrometeorites. *Geochimica et Cosmochimica Acta* 212, 196–210. https://doi.org/10.1016/j.gca.2017.05.008